JOURNAL OF AIRCRAFT
Vol. 45, No. 4, July–August 2008

Experimental Investigation of Pressure Measurement and Airfoil Characteristics at Low Reynolds Numbers

Lance W. Traub* and Evan Cooper†
Embry-Riddle Aeronautical University, Prescott, Arizona 86301

DOI: 10.2514/1.34769

A low-speed wind-tunnel investigation is presented that elucidates the effects of pressure tapping layout on observed pressure distributions. The characteristics of a 16% thick S8036 profile used in the study are explored. The set Reynolds number *Re* range was 75,000, 100,000, 150,000 and 200,000. Effects of streamwise, inclined, and wing-root taps were studied. Results encompassing pressure plots, lift coefficients, and surface flow visualization are presented. All data are compared to numerical predictions using Xfoil. The data show good agreement between experiment and Xfoil for most cases; most disagreement is in the location and extent of the laminar separation bubble. The results show that the streamwise taps may cause premature transition depending on the test Reynolds number and wing incidence. For a given angle of attack, agreement between the streamwise and inclined pressure ports improved with the Reynolds number, while for $Re \leq 100,000$, the accord improved with wing incidence. Tappings at the wing root generally indicated reduced pressure compared to those along the span, although agreement between all three tap locations was reasonable downstream of the bubble reattachment. As cited in the literature, the effect of increasing Reynolds number was to shorten the laminar bubble, not by altering the location of laminar separation but by earlier transition and reattachment. Incidence was noted to move the bubble toward the leading edge and to reduce its length slightly. Both the laminar and turbulent sections of the bubble were seen to demonstrate Reynolds number dependency. Reynolds number effects were also present in the magnitude of the loading upstream of bubble reattachment, but were not evident from the location of reattachment aft.

Introduction

EVER increasing interest and application in the use of small unmanned aerial vehicles (UAVs) has elevated research into the aerodynamics of these craft from the realm of academic to applied. UAVs have seen increasing application for reconnaissance and other duties where a small low value asset not only represents an acceptable loss, but in many cases due to small size, performs the required task better than larger vehicles. These aircraft or rotary wing vehicles fly at low Reynolds numbers, often less than 150,000–200,000, depending on the design.

An increasing body of knowledge exists on low Reynolds numbers flows [1–5]. Studies have been undertaken to understand the physics of the flow, effects of laminar separation and bubble formation, as well as studies of effective planforms in these regimes [6,7]. Generally, for Reynolds numbers less than 70,000 the flow is laminar, and methods to initiate transition are not effective. The length of the laminar separation bubble is typically longer then the length of the airfoil aft of the separation line, so reattachment does not occur. A rough airfoil surface is most effective in this regime [1]. Low Reynolds number airfoil design is complicated by the poor separation resistance of the laminar boundary layer. As the Reynolds number is increased to 100,000, methods to initiate transition may become effective. Observations typically show bubbles of the order of 20–30% of the chord. Bubble reattachment is achieved through transition of the free shear layer to turbulence which, through entrainment and enhanced mixing, facilitates attachment. The significant extent of the bubble generally alters the pressure distribution around the airfoil. As the angle of attack is increased, the bubble usually moves forward (due to the increasing pressure recovery demands aft of the minimum pressure location) but stays approximately constant in length [2]; the onset of trailing-edge separation may cause the bubble to move significantly upstream and shorten [3]. As the Reynolds number is increased, a short bubble may form that has a lesser effect on the local pressure distribution. Generally, an increase in Reynolds number results in a shortening of the bubble; the laminar separation point stays approximately constant but the reattachment point moves upstream [2,3]. However, increasing angle of attack may see this short bubble "burst," forming either a long bubble or failing to reattach at all [1]. This results in a sharp or abrupt stall with significant lift, moment, and drag implications. Measured pressures under the laminar extent of the bubble are generally constant with little fluctuation of the instantaneous pressure [2]. Pressure fluctuation levels are the greatest under the bubble aft of the shear layer transition region and upstream of reattachment, that is, in the pressure rise region [2]. Following shear layer transition, surface pressures show an adverse gradient due to expansion and deceleration of the external flow over the turbulent bubble extent.

For $Re > 200,000$, the design of an airfoil devoid of bubbles is feasible, achieved by initiating transition upstream of the adverse pressure gradient. Nonetheless, the performance of the airfoils in this regime is still inferior to that at higher Reynolds number, as the separation resistance of the turbulent boundary layer increases with the Reynolds number.

Quantitative airfoil measurements at low Reynolds number are usually recorded using a specialized force balance [7] if global forces and moment are desired or pressure tappings if details of the load distribution as well as integrated lift and moment are required. Flow diagnostics may be accomplished using surface visualization techniques (e.g., titanium dioxide or oil flow) or off-surface methods, hydrogen bubble, [8] or smoke. A difficulty in the measurement of pressure is the potential effect the tapping's themselves may have on the flow. For this reason, tappings are often laid in diagonals across the wing planform for two-dimensional studies. Occasionally, for simplicity, tappings are placed at the wing root of a two-dimensional model that may be used for educational purposes. Consequently, the measurements are immersed in a junction flow.

In this paper, high accuracy pressure measurements are presented over a S8036 airfoil at Reynolds numbers from 75,000 to 200,000.

Received 24 September 2007; revision received 19 November 2007; accepted for publication 22 November 2007.

*Associate Professor, Aerospace and Mechanical Engineering Department. Member AIAA.

†Undergraduate Student, Aerospace and Mechanical Engineering Department.

The effect of pressure tapping orientation and location is explored using direct measurement as well as surface flow visualization. Pressure profiles and lift curve plots are compared with numerical solutions using Xfoil. The study aims to explore the potential effect that the tappings may have on the measured pressures, as well as provide experimental insights into low Reynolds number behavior and a database for computational comparison.

Equipment and Procedure

A low-speed 1 ft × 1 ft open return wind tunnel was used. Wings were designed in CATIA and then rapid prototyped using Embry-Riddle's rapid prototyping facilities yielding acrylonitrile butadiene styrene (ABS) plastic wing representations. Three 101.6-mm chord, c, wings were manufactured: one which was pressure tapped, another which was also tapped but was used for surface flow visualization, and a third which was not tapped, labeled the "clean" wing. The wing section was a S8036 with a thickness of 16%. The profile was chosen due to its good performance at low Reynolds numbers (such that the wing section may be representative of what would be used in this regime). It was also selected due to its reasonable internal volume which was necessary due to the quantity of pressure tappings in the wing. The wings spanned the tunnel to facilitate two-dimensional flow. As shown in Fig. 1, tappings were located at the root as well as at 40% of the span. At the 40% location two tapping sets were located: one streamwise, that is, straight aft, and the other inclined at 30 deg. The tappings located at 40% were organized in the displayed overlapping pattern to mitigate the potential for any spanwise gradients to be misinterpreted as port effects. For each tapping orientation or location, a total of 30 taps were used, 20 on the upper surface and 10 on the lower surface. The tubing used for the ports located from the nose to 20% chord had an internal diameter of 0.25 mm. Tubing located aft of this location had an internal diameter of 0.5 mm. Smaller tubing was not used due to an extremely slow response time and the high probability of tapping obstruction. Great care was taken to ensure that the taps were clean and did not protrude from the surface. The taps were formed by passing Tygon® tubing of the appropriate internal diameter through a preformed location hole in the rapid prototyped wing surface. The tubing was then bonded in place on the inside of the wing and then cut to length using a thin blade held parallel to the surface. This method resulted in cleanly formed pressure taps that were flush with the surface. This was checked both tactilely and using a 10x magnification loupe. Locations of the pressure taps for rows A, B, and C are as follows: $x/c)_u = 0, 0.015, 0.05, 0.075, 0.1, 0.125, 0.15, 0.175, 0.2, 0.25, 0.3, 0.35, 0.4, 0.45, 0.5, 0.55, 0.6, 0.7, 0.8$, and 0.9; $x/c)_l = 0$, 0.0175, 0.1, 0.15, 0.2, 0.3, 0.4, 0.5, 0.6, 0.7, and 0.8, where x and c correspond to locations along the chord length, respectively. u and l correspond to the upper and lower surfaces, respectively.

In this investigation, the accuracy and repeatability of the pressure measurement system is paramount, especially considering the low magnitudes of the pressures recorded. Consequently, an electronic pressure scanner was designed and built in-house. The scanner consists of 30 independent temperature compensated differential pressure transducers. The transducers are connected through solenoid valves to the measurement ports. A custom interface was written in Visual Basic to control the valves as well as process and record the measured pressures. The valves were used to facilitate automatic zeroing of the transducers while running, eliminating any null or thermal offset effects. The pressure transducer outputs were digitized using a 32-channel 16-bit National Instruments external USB analog-to-digital converter board. The board allows scanning of the pressures at up to 250, 000 readings/s. All presented pressures are the average of 1000 readings. Calibration of the scanner was performed using a FlowKinetics™ LLC FKT 1DP1A-SV pressure/flow meter. The FKT meter is calibrated against a dead weight primary standard and was within its calibration specifications. Comparison with the standard showed accuracy of better than 0.5 Pa. Calibration and comparison of the scanner with the FKT meter showed measured pressure agreement within 0.8 Pa for all 30 of the transducers. The uncertainty interval for the pressure coefficient Cp was estimated using the method of Kline and McClintock [9]. The worst case uncertainty ($Re = 75,000$ and a large angle of attack, AOA) yielded an uncertainty of $w_{Cp} = 0.028$ or $w_{Cp}/Cp = 1.8\%$.

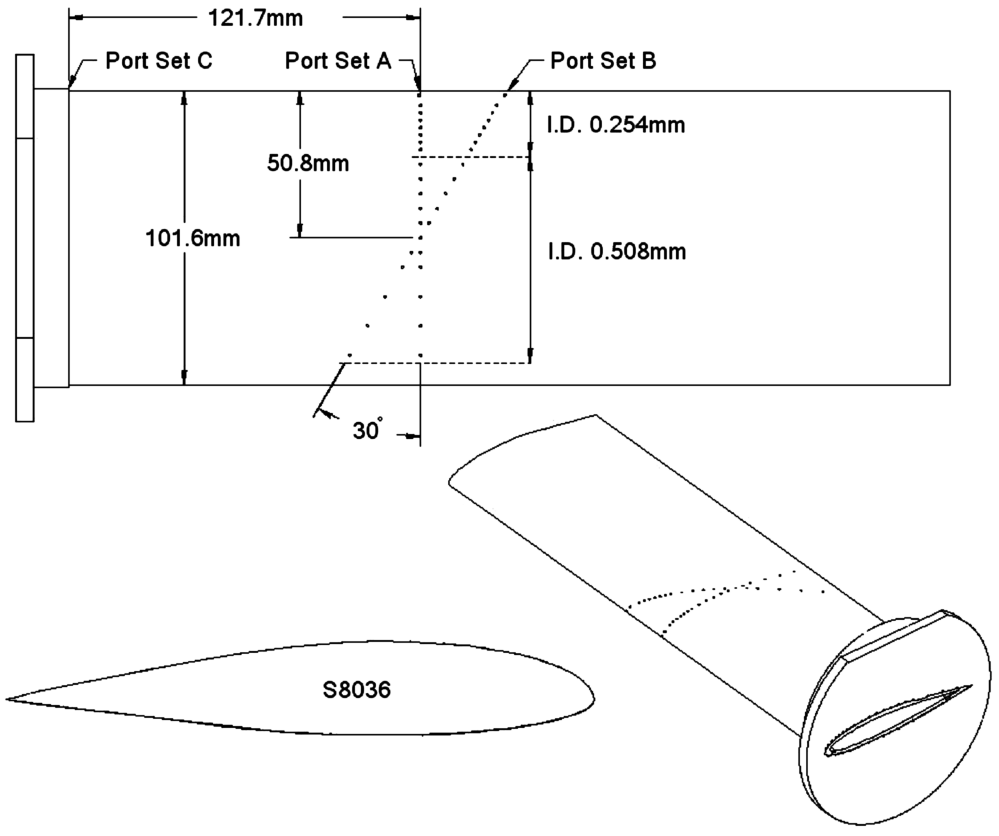

Fig. 1 Model geometry and port layout.

Surface flow visualization was performed using a mixture of titanium dioxide, paraffin, linseed oil, and oleic acid. The wing was set at the desired AOA, the mixture was applied using a brush, and the tunnel was rapidly increased to the desired Reynolds number. The fluid motion was observed to aid in interpretation while still and video images were recorded. Random test conditions were repeated to determine pattern repeatability. Surface visualization was undertaken for AOA = 4 and 14 deg.

The tunnel freestream velocity was measured using the FlowKinetics^{TM} LLC FKT 1DP1A-SV meter. This meter measures atmospheric pressure, temperature, and relative humidity, all of which are used to compute the density used in the velocity calculation. Meter accuracy is specified by the manufacturer as better than 0.1%. The wing angle of attack was set using a Mitutoyo 3600 digital protractor with a resolution of 0.01 deg. Wing set repeatability was also found to be within 0.1 deg. As the tests are essentially comparative, no corrections for wall effects were applied. Additionally, as the results may be used for computational comparison, wall effect corrections (especially with separation present) were not applied as their applicability may be questionable.

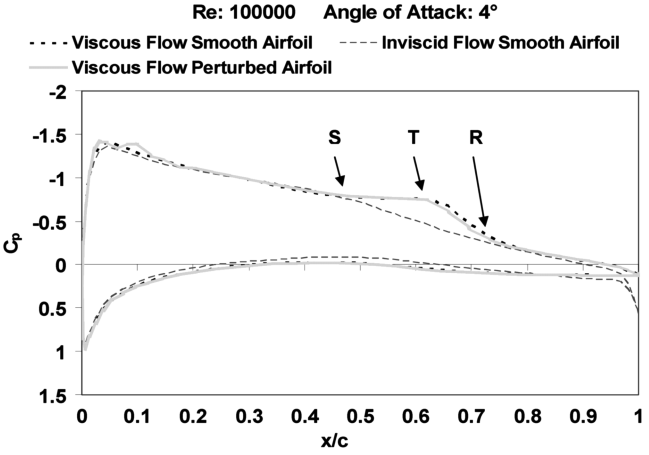

Fig. 2 Effect of surface perturbation on calculated pressure distribution.

Results and Discussion

The following results summarize pressure measurements and observed flow features at the three port sets A, B, and C over the wing at Reynolds numbers of 75,000, 100,000, 150,000, and 200,000. The wing was pitched through an angle of attack range from −4 to 16 deg in 2-deg increments. Results are presented in conjunction with flow visualization to enhance and simplify trend observation. Initial pressure results showed small undulations near the nose of the airfoil. These undulations were traced to small "ripples" near the airfoil nose, caused by the manufacturing process. To verify these possible coordinate effects, the estimated surface displacements were used to modify the airfoil's geometric profile used in Xfoil. The results are shown in Fig. 2 (perturbed legend). The modified coordinates were at upper surface chord locations of 8.1 and 10.2%, with the y coordinate increased by 0.069 and 0.084 mm, respectively. The numerical data in Fig. 2 also include the unperturbed airfoil as well as an inviscid calculation. The results indicate that the effect of the nose perturbations are localized, although bubble reattachment may occur slightly sooner. The inviscid solution shows slightly reduced loading near the leading edge compared to the viscous solution. Presented on the plot are the locations of initial bubble separation (S), transition to turbulence (T), and reattachment (R). Notice that after transition the bubble sustains pressure recovery due to expansion of the external flow over the contracting bubble, although the flow has not yet reattached.

Figures 3–11 present summaries of the measured pressures over the wing at four Reynolds numbers and three angles of attack. A systematic series of data is included for completeness and to aid computational comparison. Where recorded, flow visualization images are included to aid in interpretation. Figure 3 (AOA = 4 deg and $Re = 75,000$) shows reasonable agreement between predictions (Xfoil) and the port sets A and B. Bubble extent agreement is also good. The root tappings, C, show poor accord near the leading edge and from the midchord aft. This may be due to the horseshoe vortices [10] that form in the leading-edge vicinity having the closest surface proximity. Acceleration around the leading edge may stretch the vortices, increasing their peak vorticity and reducing their diameter. Pressure recovery may have the opposite effect, axially retarding the vortices, increasing their size, and displacing them further from the surface such that their induced effect on the junction flow reduces. Increasing Reynolds number to 100,000 (Fig. 4) shows improved correlation between the port sets. As seen in Fig. 3, root tapping agreement is good in the pressure recovery region ahead of laminar separation. Xfoil shows good agreement as to bubble location and extent with the experimental data although the magnitude of the upper surface pressures are greater than experimentally indicated. Surface visualization shows (the dotted lines drawn on the figure show the locations of tappings A and B; the lower inset photograph shows the clean wing without taps) that the port set A promotes

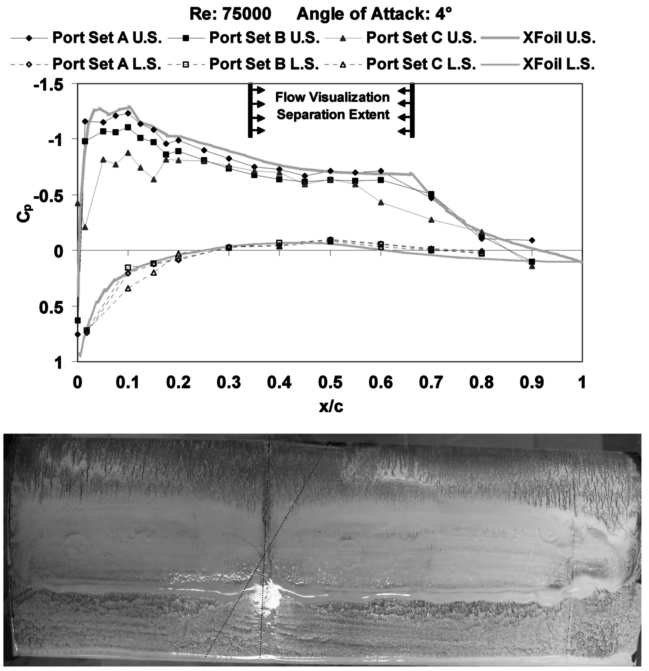

Fig. 3 Experimental and numerical pressure coefficient distributions, AOA = 4 deg, $Re = 75,000$. The lower inset shows titanium dioxide rendered skin friction patterns. Dotted lines show the location of pressure ports A and B.

transition, visually splicing the laminar bubble. Nonetheless, the recorded pressure data does indicate effects analogous to that associated with a bubble.

Increasing Reynolds number to 150,000, Fig. 5, improves agreement between the experimental data and Xfoil for sets A and B. The root tappings C show poorer accord with the other tapping sets. This may be due to an increase in the strength of the junction flow horseshoe vortices with Reynolds number. The inset flow visualization and pressure data show a shortening of the bubble as the Reynolds number increases (compare Figs. 3 and 4). The visualization suggests that transition due to tapping set A visually eliminated the separation in the vicinity of the ports, although a small extent separation is evident in the pressure signature. The wing wall junction shows evidence of the time averaged passage of a vortex (as shown on the right-hand side) as well as a separation region between the vortex and side wall. Note that transition near the right-hand side of the wing is due to a joining between the main wing panel and an extension piece (the wing was not manufactured to the full width of

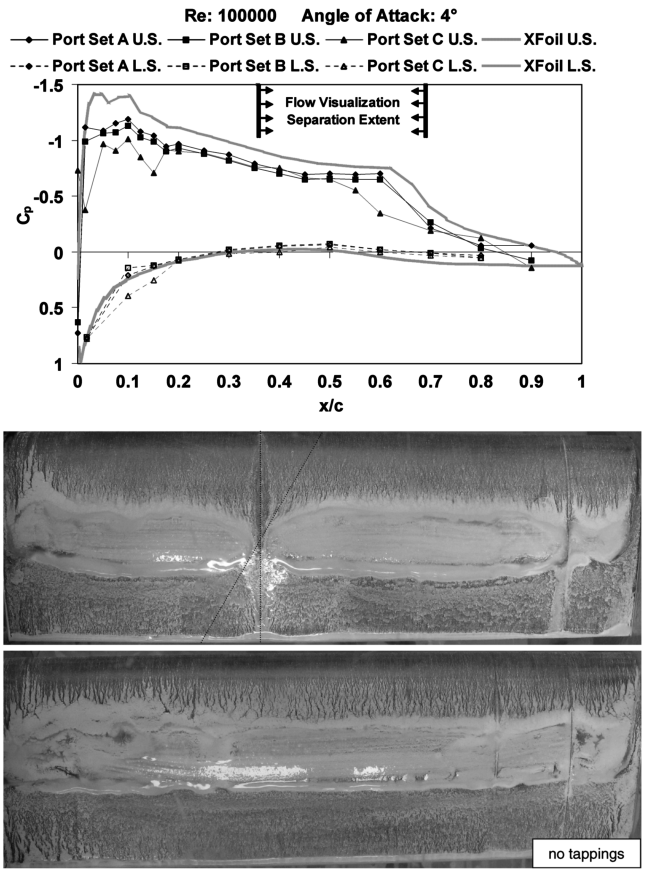

Fig. 4 Experimental and numerical pressure coefficient distributions, AOA = 4 deg, $Re = 100,000$. The lower insets shows titanium dioxide rendered skin friction patterns.

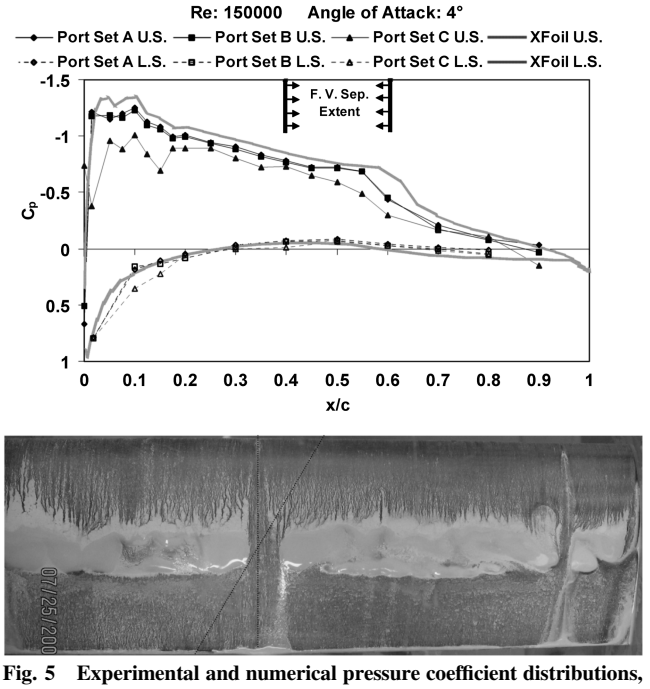

Fig. 5 Experimental and numerical pressure coefficient distributions, AOA = 4 deg, $Re = 150,000$. The lower inset shows titanium dioxide rendered skin friction patterns.

the tunnel requiring a short wing extension piece to facilitate the 1-ft span).

For this AOA (4 deg) increasing the Reynolds number to 200,000 shows excellent agreement between Xfoil and tapping sets A and B

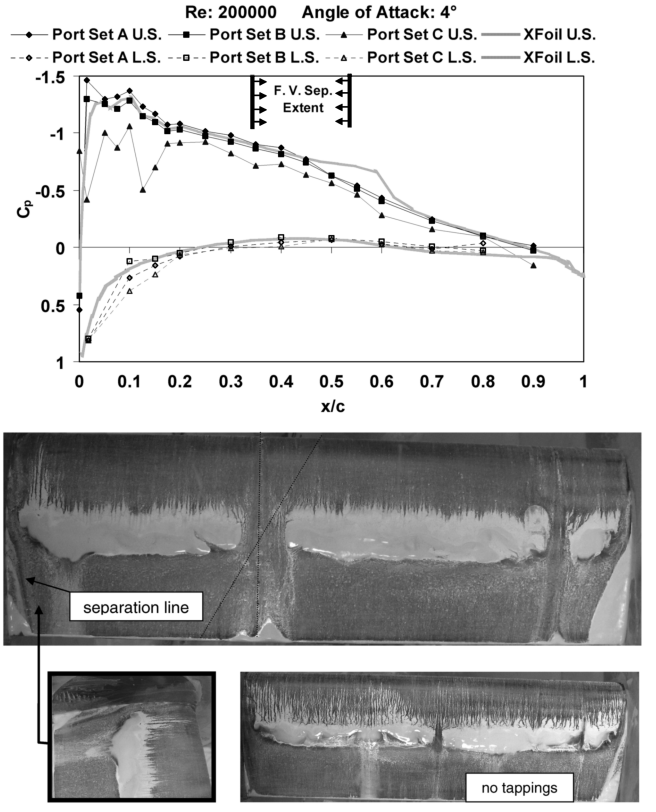

Fig. 6 Experimental and numerical pressure coefficient distributions, AOA = 4 deg, $Re = 200,000$. The lower inset shows titanium dioxide rendered skin friction patterns.

(see Fig. 6). However, Xfoil predicts the presence of a short bubble between approximately 45–62% chord. This is not evident in the experimental pressure trace. The flow visualization data show that a bubble does indeed exist, but is locally eliminated by the flow transition caused by the taps. Notice that tap set B does not cause apparent transition. Thus the disturbances created by the staggered ports do not amplify sufficiently to cause transition at these Reynolds numbers and AOA. However, the cumulative disturbances from port set A do amplify sufficiently to cause transition and are not attenuated by viscous dissipation. Note that the flow in the tapping vicinity then appears to exhibit localized turbulent trailing-edge separation. The data clearly indicate that the effect of the taps has a Reynolds number dependency, which lessened the effect at lower Reynolds numbers (for this wing, experimental setup, and test conditions) (see Figs. 3–6). The measured separation bubble location as indicated by the skin friction patterns is upstream of the numerical estimate. This may be in part due to surface paint estimates indicating separation prematurely, as the paint flow tends to stagnate before the surface skin friction tends to zero [11]. Squire [11] conducted a study of the flow of a thin oil sheet under the boundary layer of a body. His analysis showed that the effect of the oil on the boundary layer motion is marginal and that pressure gradients do not affect the oil flow except for regions where skin friction is low, that is, separation zones. Thus, inferences on exact locations of flow separation inferred from surface flow studies must be treated cautiously. Comparing the Xfoil and experimental data indicates that the effect of the bubble is localized and has little effect on the pressure upstream or downstream of separation and attachment. The skin friction patterns (lower photograph is for the clean wing) show the separation line associated with the passage of a junction horseshoe vortex, labeled as "separation line," Fig. 6. This vortex and the resulting low energy confluence of the wing and wall boundary layers have the effect of causing large extents of root separation in the vicinity of the greatest pressure recovery region, $x/c > 0.5$. The junction flow also has the effect of displacing the separation bubble from the wall as well as tapering or contracting it toward the aft section of the bubble. This may be due to turbulent flow propagating from the root junction closing the separation.

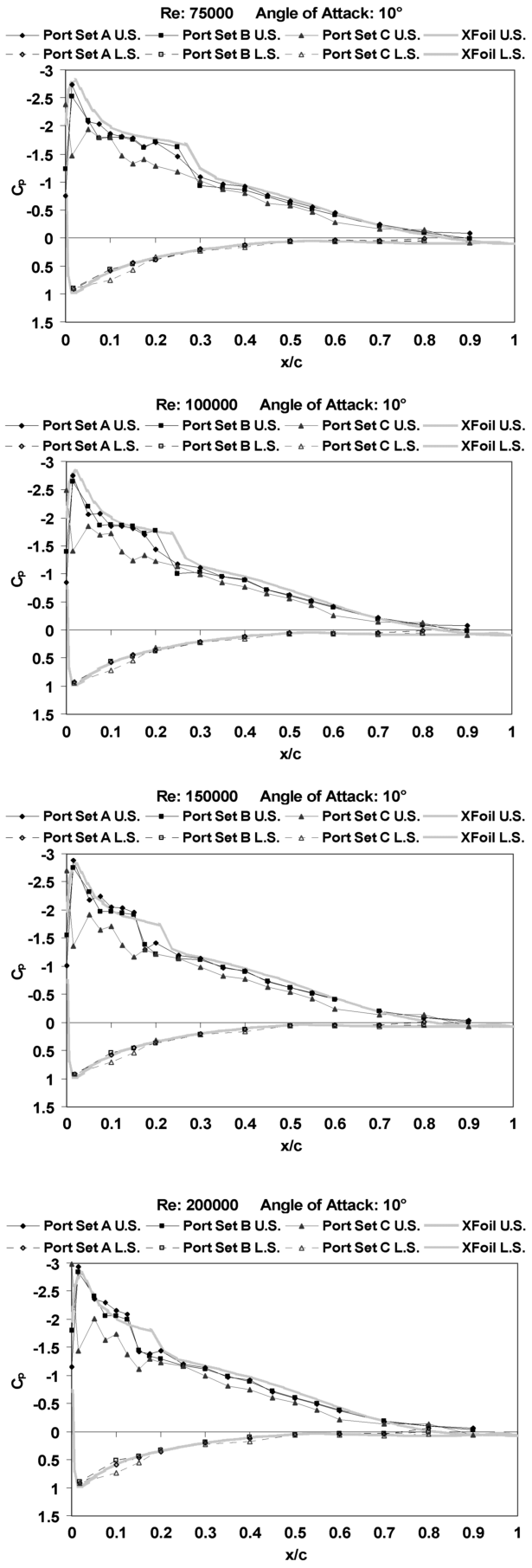

Fig. 7 Effect of Reynolds number on measured pressure coefficient; AOA = 10 deg.

Effects of the Reynolds number for AOA = 10 deg are presented in Fig. 7. The figures show a forward movement of the bubble with the increase in AOA; compare with Figs. 5 and 6. Peak suction increases slightly with Reynolds number. The reattachment location moves upstream with increasing Reynolds number resulting in a shorter bubble. The length of the transition region and subsequent reattachment appears to also shorten with an increase in Reynolds number. The plateau in Cp, indicative of the laminar extent of the separation bubble, shows an increasing gradient with Reynolds number. This suggests the bubble experiences pressure recovery in this region. An explanation may be a thinning of the vertical height of the bubble with Reynolds number, allowing expansion of the external flow.

Ports A and B show good overall agreement with Xfoil predictions. Xfoil does tend to indicate a longer bubble then the experimental data as Reynolds number increases, which may be due to tap induced transition. An increase in Reynolds number may reduce the stability of the laminar boundary layer and increase its susceptibility to transition caused by disturbance amplification. Interestingly, all three port sets show reasonably close accord aft of the bubble reattachment region, despite the root junction flow.

Figures 8–11 explore the effect of increasing the set AOA to 14 deg. For $Re = 75,000$ and 100,000 the experimental traces show massive upper surface separation, clearly seen in the surface skin friction patterns. Notice that the numerical results do not agree with experimental for not only the suction surface, but the pressure surface too. Increasing the Reynolds number to 150,000 and 200,000 shows good agreement between port sets A and B and Xfoil. The traces show the presence of a short bubble near the leading edge followed by an extent of attached turbulent flow and then trailing-edge separation. The surface flow data show the leading-edge short bubble as well as the trailing-edge separation. For $Re = 150,000$ (Fig. 10) the trailing-edge separation extent indicated by the surface flow is greater than suggested by the pressure data or Xfoil. The surface flow patterns shown in Fig. 11 are for the same conditions (AOA = 14 deg, $Re = 200,000$), yet the patterns are dissimilar. The upper pattern is consistent with the pressure and numerical data. The lower pattern was observed over the clean wing with no ports. To further study the patterns, additional tests were run and videoed to establish the temporal flowfield evolution. The result is shown in Fig. 12. Images were acquired after the tunnel had been running for

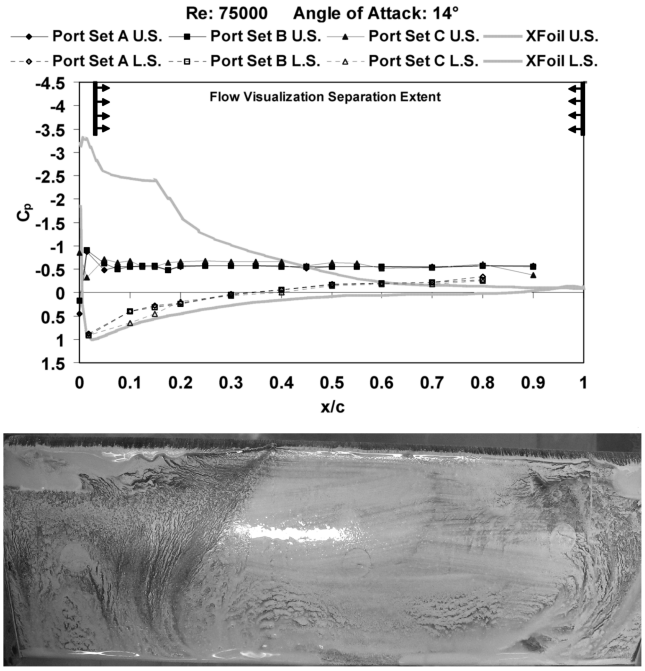

Fig. 8 Experimental and numerical pressure coefficient distributions, AOA = 14 deg, $Re = 75,000$. The lower inset shows titanium dioxide rendered skin friction patterns.

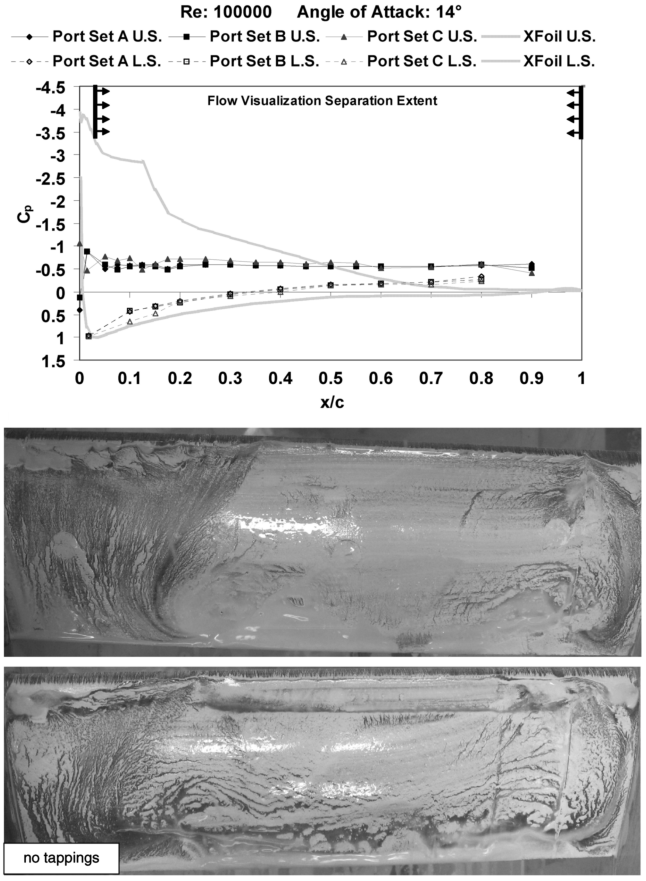

Fig. 9 Experimental and numerical pressure coefficient distributions, AOA = 14 deg, $Re = 100,000$. The lower insets show titanium dioxide rendered skin friction patterns.

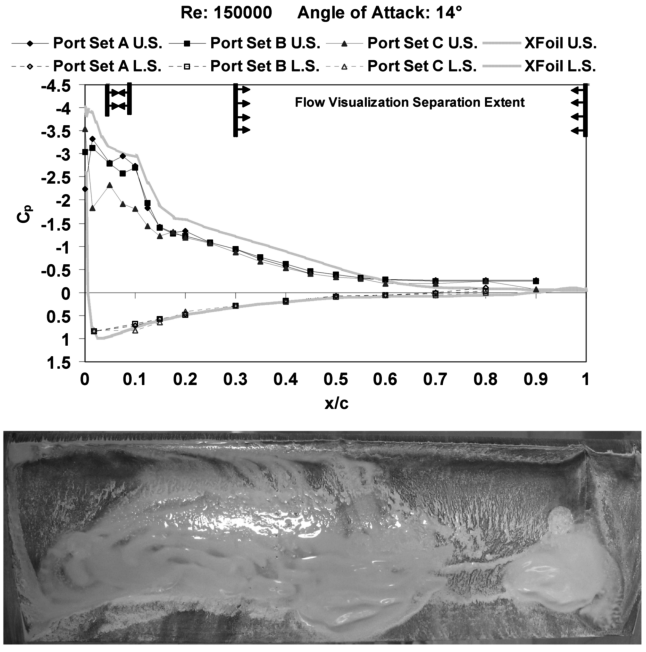

Fig. 10 Experimental and numerical pressure coefficient distributions, AOA = 14 deg, $Re = 150,000$. The lower inset shows titanium dioxide rendered skin friction patterns.

approximately 10–15 s and the surface flow had appeared to reach a time averaged steady-state condition. The sequence of figures from a) to g) was acquired over 2 s. The surface flow shows the pattern changing from one pseudoequilibrium condition to another. In

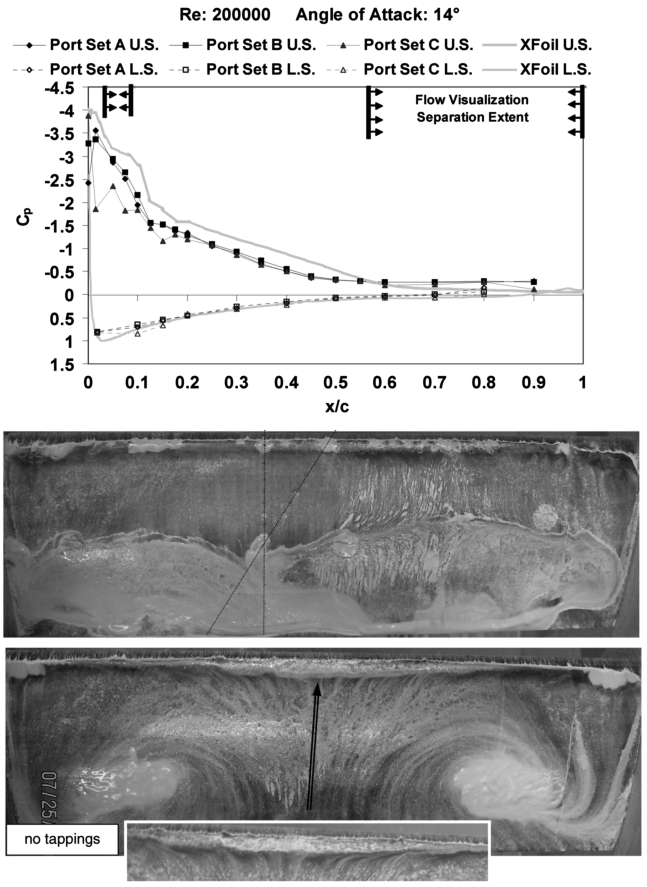

Fig. 11 Experimental and numerical pressure coefficient distributions, AOA = 14 deg, $Re = 200,000$. The lower insets show titanium dioxide rendered skin friction patterns.

Fig. 12a) the surface paint suggests a leading-edge separation which may reattach and then massive separation. The flow shows two recirculating nodes (foci) with reverse flow in between (shown with better clarity in the lower photograph in Fig. 11). The inset figure at the bottom of Fig. 11 shows that the reverse flow forms a node of separation when merging with the attaching stream surface from the leading-edge short bubble. This may then form a separated stream surface which forms the upper bound or dividing stream surface of a large separated flow cell(s). The patterns seen in Figs. 11 and 12 are similar to those reported in [12]. As image capture continued, the flow appeared to suddenly change, no longer separating just aft of short bubble reattachment. Consequently the line of massive separation moved rapidly aft. It would appear that transition and reattachment of the leading-edge bubble was successful so that attached turbulent flow is seen from approximately 10–50% of the chord. Possible causes of the observed behavior may be the effect of thinning of the surface flow mixture with time, or perhaps external influences such as tunnel vibration. The flow visualization indicates the importance of systematic and repeated testing at low Reynolds numbers to establish possible time dependency of the observed results.

Figures 13–15 summarize the observed effect of Reynolds number for AOA = 4, 10, and 14 deg for the three port sets. As shown in Fig. 13, port set A suggests elimination of the laminar separation bubble at $Re = 200,000$ and a progressive increase in upper surface loading with Reynolds number. The location of laminar separation is seen to be invariant within the resolution of the port locations; however, transition in the separated free shear layer and turbulent reattachment moves progressively upstream, shortening the bubble. The influence of the bubble is seen to be localized and does not affect the attached flow pressures. Port set B shows similar trends to those for set A (middle inset figure) except that the increase in upper surface loading is more systematic, resulting from a reduced tendency for the ports to affect transition. The root tappings, set C, show little Reynolds number effect for $Re > 75,000$. This is due to

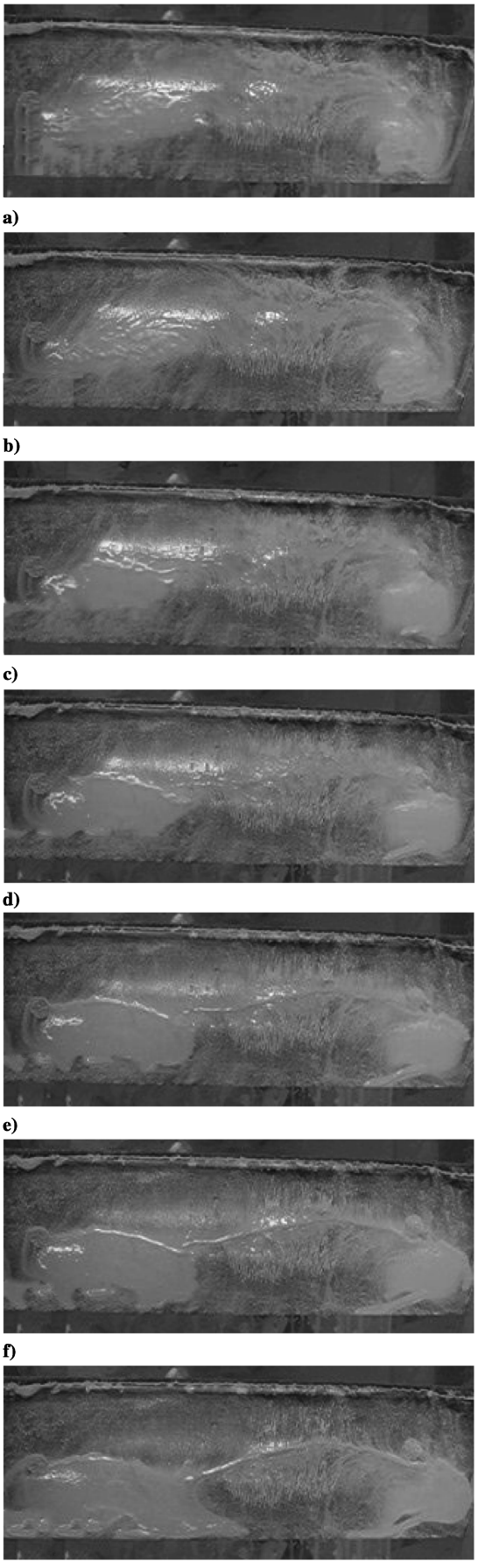

Fig. 12 Temporal flowfield evolution. $Re = 200,000$, AOA $= 14$ deg. The time interval from a) to g) is 2 s.

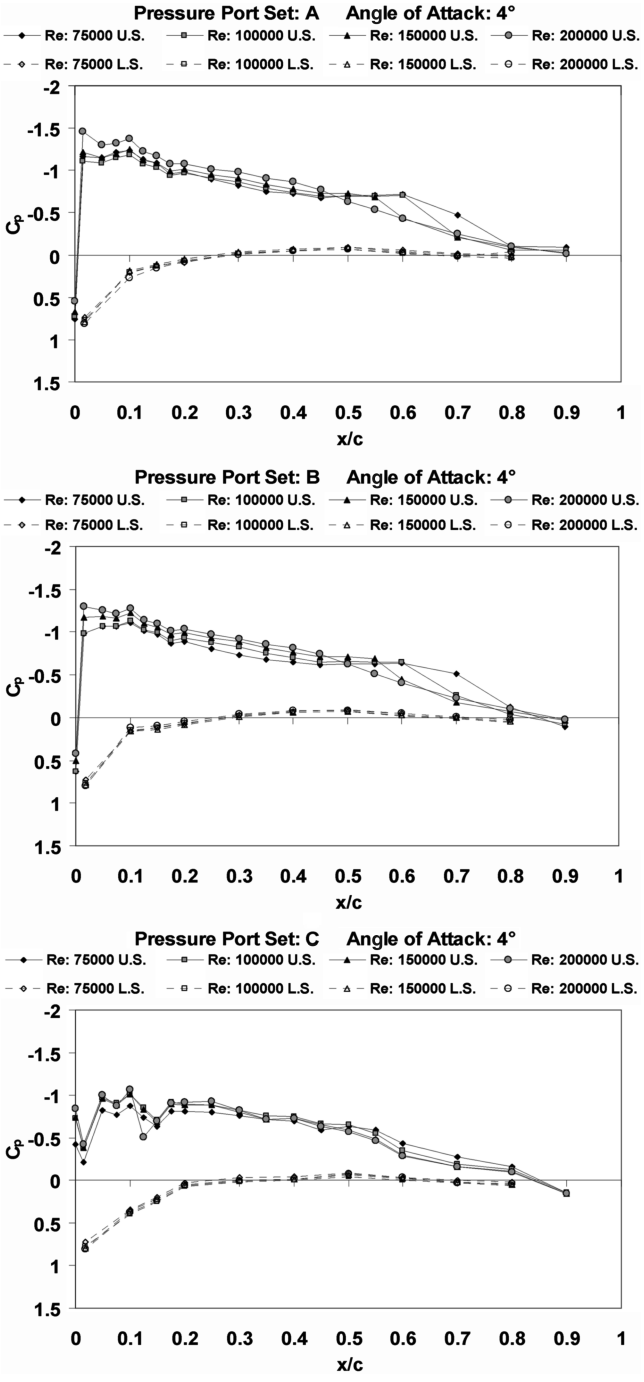

Fig. 13 Effect of Reynolds numbers on measured pressure coefficient, port sets A, B, and C; AOA $= 4$ deg.

pressures at C being affected by the confluence of the wing and turbulent wall boundary layers. Consequently, transition is always affected and not Reynolds number dependent (in the Reynolds number range investigated). Notice that the indicated pressure profile for set C is in reasonable agreement with sets A and B for $x/c > 0.3$.

Figure 14 shows a data summary for an increase of AOA to 10 deg. Port set A is shown as the top inset. Increasing Reynolds number clearly moves the bubble reattachment location upstream. The chordwise extent of pressure recovery in the transition region of the bubble is also seen to shorten. The point of laminar separation is seen to be invariant. Increasing Reynolds number steadily increases the suction peak and bubble loading although pressures in the turbulent region aft of attachment show no Reynolds number effects in the measured range. The inclined tap set B shows similar trends to that described above except that the bubbles are located further aft. Additionally, the indicated location of laminar separation is located

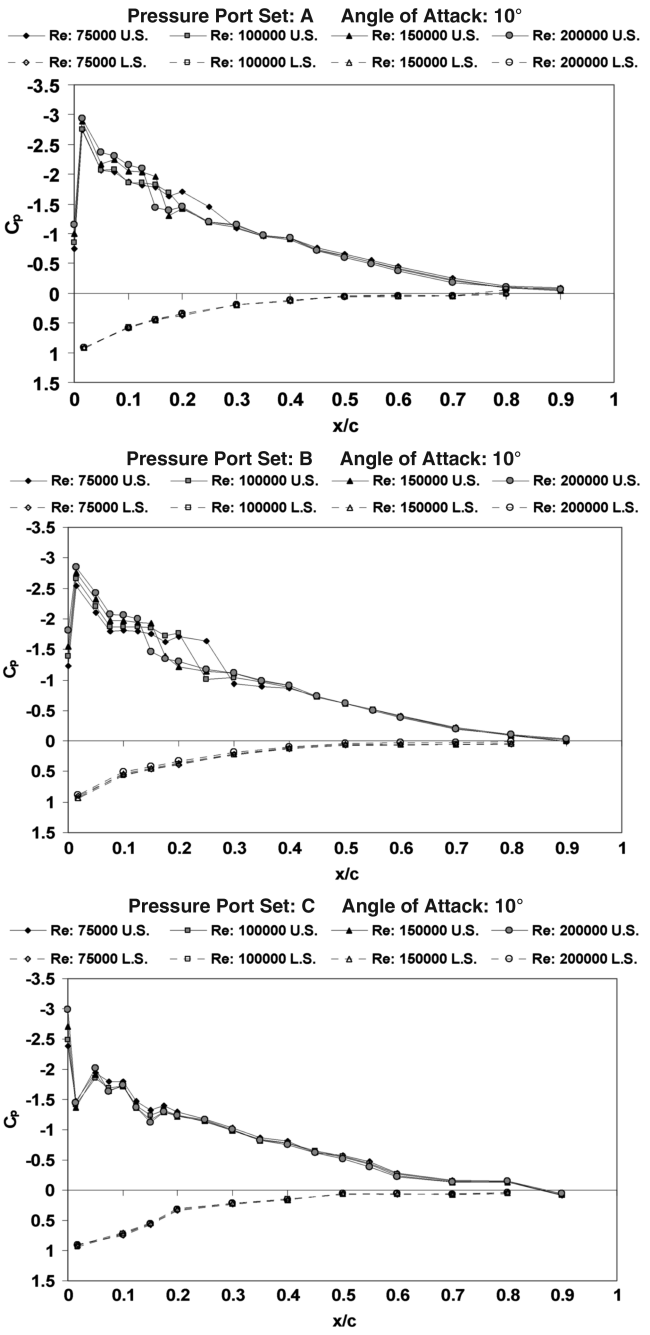

Fig. 14 Effect of Reynolds number on measured pressure coefficient, port sets A, B, and C; AOA = 10 deg.

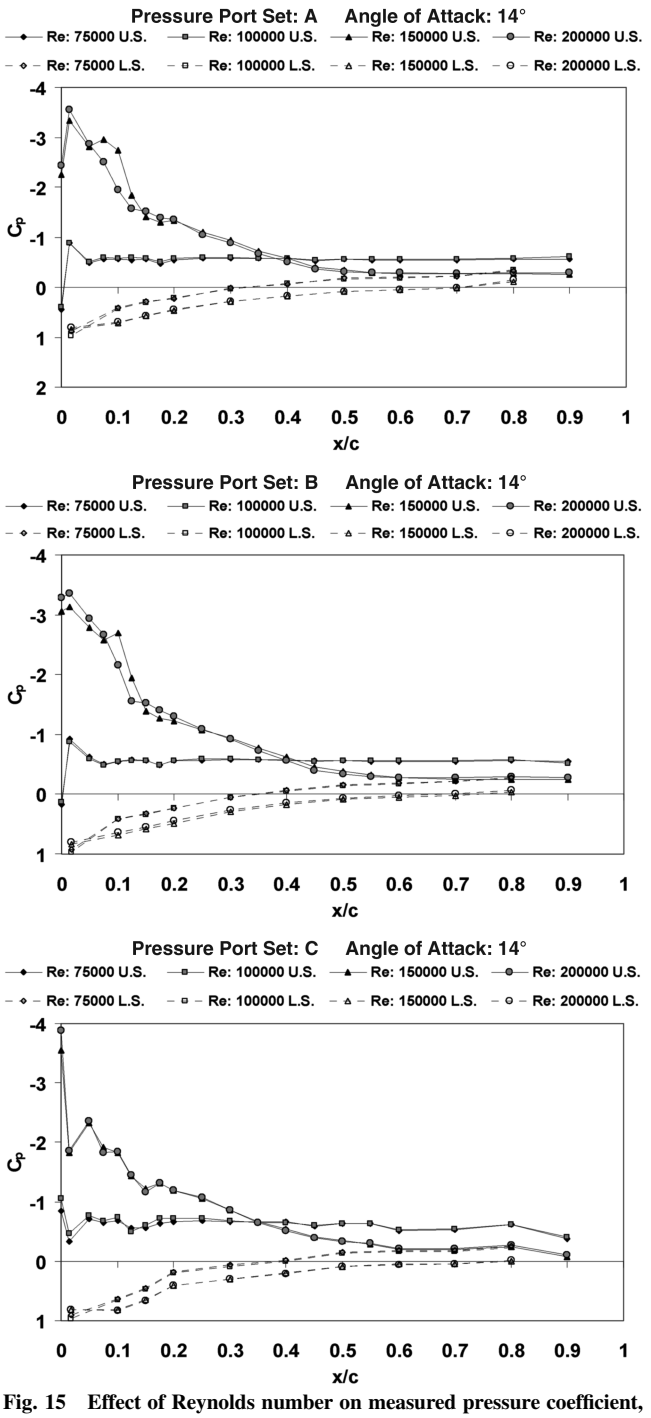

Fig. 15 Effect of Reynolds number on measured pressure coefficient, port sets A, B, and C; AOA = 14 deg.

one tapping aft (2.5%) of port set A. Bubble lengths are also somewhat different to those indicated by set A. Port set A shows some pressure recovery (gradient) under the bubbles laminar region; this is not observed for set B (notice the flat plateau). Weiburst et al. [2] observed similar results for an increase in Reynolds number over their profile. A consequence of the inline taps, A may then be able to simulate a somewhat higher Reynolds number flow. The root tappings, C, show little Reynolds number effect as the merged junction boundary layer is already turbulent. An AOA of 14 deg (see Fig. 15) shows significant Reynolds number effects for all port sets in the vicinity of the leading edge. The shape and peak suction values are different between sets A and B. The root taps are once again somewhat representative from approximately 30% of the chord aft. The results show that the laminar and transitional extent of the bubble show Reynolds number dependency. Reynolds number effects were also present in the magnitude of the loading upstream of bubble reattachment, but were not evident from the location of reattachment aft.

Figure 16 investigates the effect of increased incidence on loading. Thin airfoil theory shows that the pressure differential across the wing at a chordwise location varies proportionally to the incidence. For comparison, measured loads at AOA = 2 and 4 and 4 and 8 deg were reduced by their respective incidence. The results show reasonable collapse of the data, except near the trailing edge.

The bubble location and extent is investigated in Fig. 17 for $Re = 75,000$, 100,000, and 150,000. Data were difficult to discern for $Re = 200,000$ and are not included. The plots resemble those presented in [3]. The shortening of the bubble with increasing incidence and Reynolds number is clearly apparent. Studies [1] have suggested that bubble length does not change with AOA, but the present data indicate a weak dependency. An increase in AOA shows a forward movement of the laminar separation point, essentially linearly for $Re = 75,000$. For the higher Reynolds numbers, the forward movement is approximately invariant with AOA (plateau)

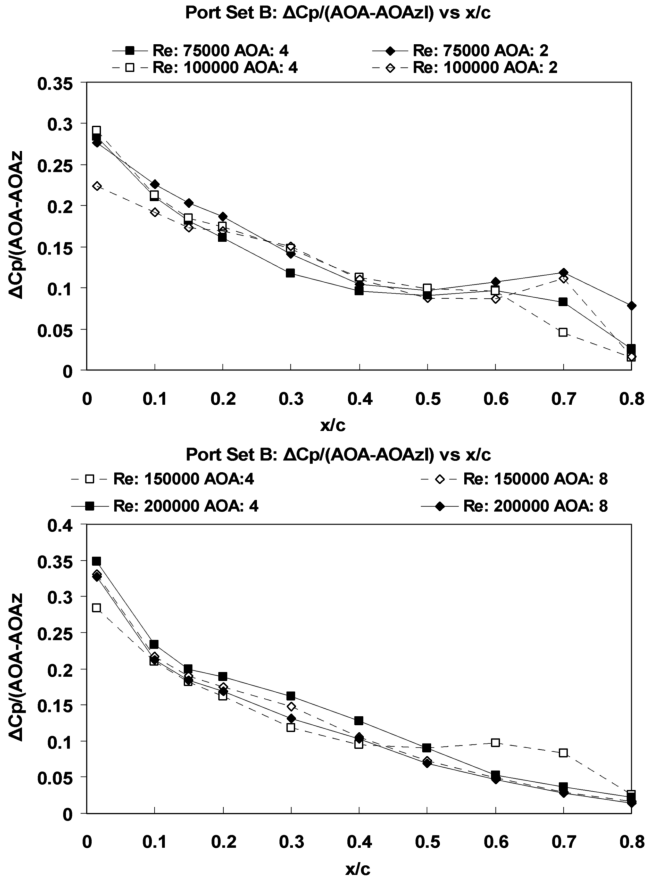

Fig. 16 Variation of ΔCp with AOA, port set B.

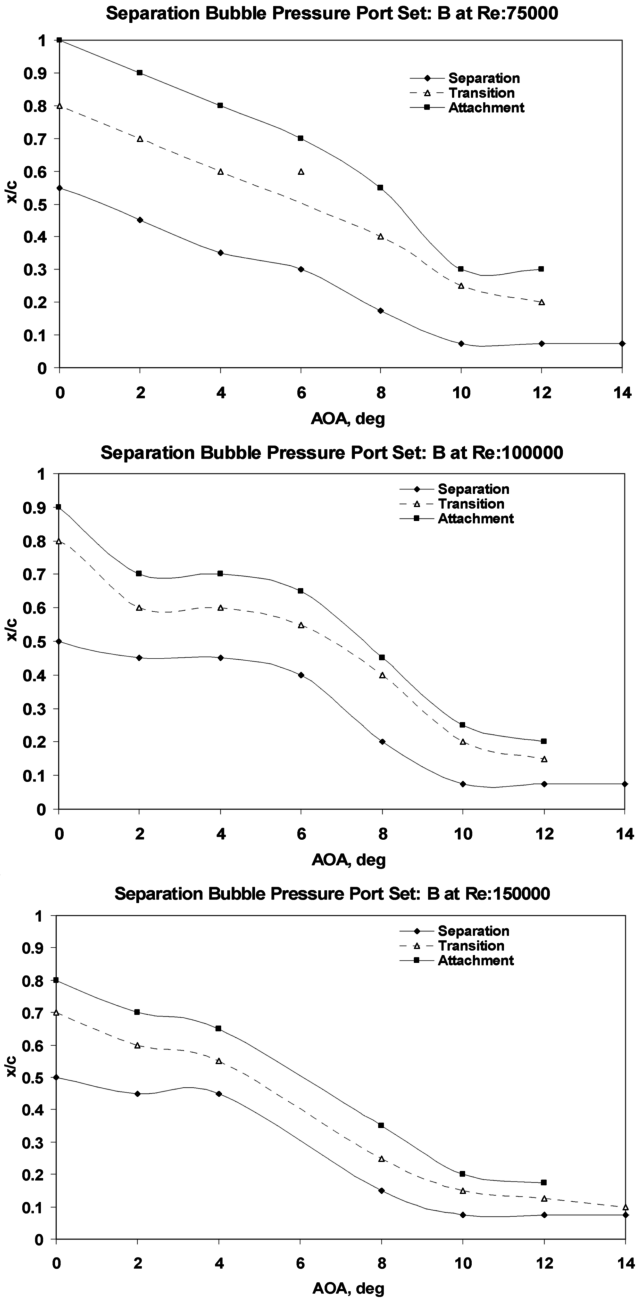

Fig. 17 Effect of Reynolds number and AOA on measured bubble geometric properties.

and then moves forward rapidly; this plateau AOA extent reduces as the Reynolds number increases (approximately 6 and 4 deg for $Re = 100,000$ and 150,000, respectively). Analysis of the Cp plots for these and surrounding AOAs (not included for space considerations) showed a proportionally larger increase in the upper surface suction peak and pressure recovery demands (adversity of the pressure gradient) in going from 6 to 8 deg ($Re = 100,000$) and 4 to 6 deg ($Re = 150,000$) than in any other 2-deg increment. Consequently, this causes a forward movement of the separation line. For all presented Reynolds numbers, the separation, transition, and reattachment location appear to show little movement for AOA > 10 deg, concurrent with the onset of trailing-edge stall. Incidence does not appear to affect the relative location of transition relative to the length of the bubble; transition appears to occur at approximately 50–65% of the bubble length. For higher incidence, >10 deg, the onset of trailing-edge separation appears to move transition somewhat aft with respect to the bubble length.

Figure 18 presents a comparison of the present data, Xfoil, and a Fluent simulation for $Re = 100,000$ and AOA = 4 deg. The computational fluid dynamics (CFD) grid used 2×10^6 cells while the computations used a k–ω shear stress transport (SST) turbulence model. A transitional flow option was enabled to allow the prediction of transition. Convergence was achieved after 857 iterations. Agreement between Fluent and experiment is seen to be encouraging. The extent and pressure recovery associated with the bubble is somewhat underpredicted. Figure 19 presents computations of the vorticity and turbulence (based on the streamwise velocity fluctuation). The figure shows significant vorticity dissipation associated with the bubble as well as the displacement of the near wall vorticity away from the wall. Turbulence levels are highest just after the location of shear layer transition (approximately $x/c = 0.56$, see Fig. 18) and are confined to an off-surface band. Closure of the bubble and subsequent turbulent reattachment shows a thick turbulent wake which appears to locally affect the pressure surface near the trailing edge. Computed surface shear stress is

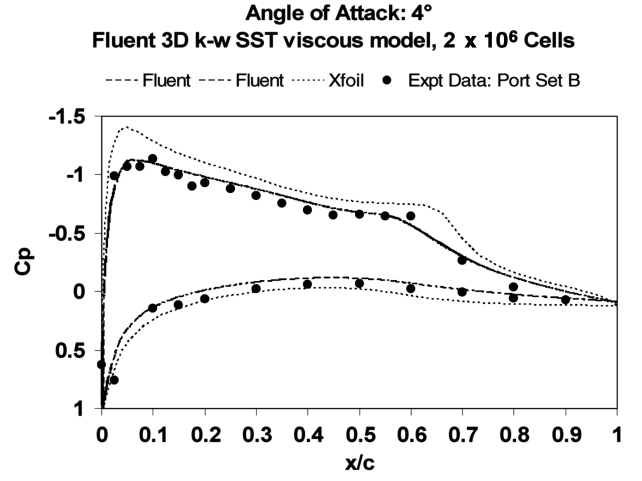

Fig. 18 Comparison of Fluent, Xfoil, and experimental data, AOA = 4 deg, $Re = 100,000$.

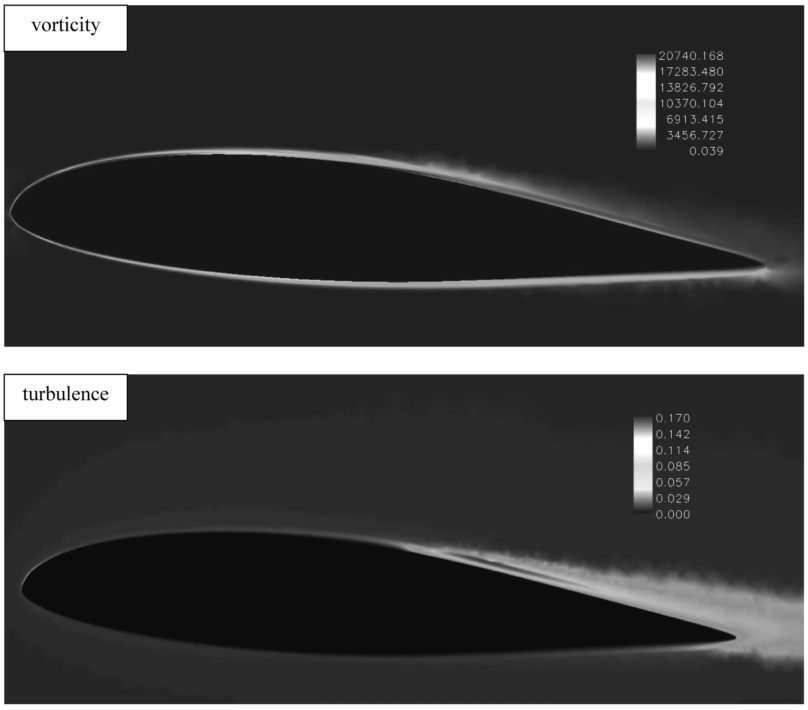

Fig. 19 Fluent renderings of vorticity and turbulence (based on the x velocity fluctuation). AOA = 4 deg, $Re = 100,000$.

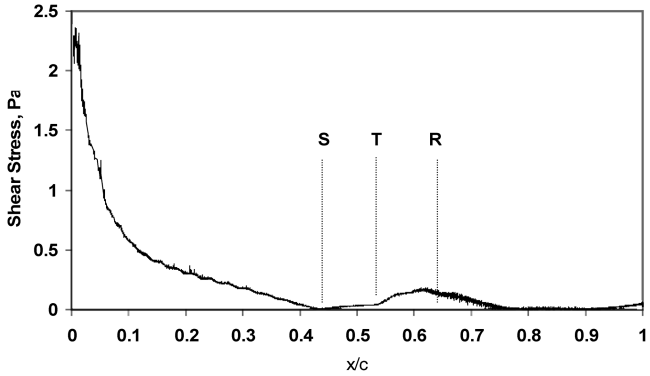

Fig. 20 Computational estimate of upper surface shear stress. AOA = 4 deg, $Re = 100,000$.

shown in Fig. 20. As expected, separation (S) is associated with the approximately zero shear stress. The stagnant laminar region of the bubble also shows minimal shear stress. Transition (T) through mixing and entrainment greatly reenergizes the flow increasing shear. Notice that shear under the transitioned bubble represents a local maxima. Shear subsequently reduces rapidly as the turbulent boundary layer that forms after reattachment is often thicker and of lower momentum than one that forms in an attached transition process. The low magnitude of the shear stress after attachment may suggest that trailing-edge separation is imminent.

Integrated loads are displayed in Fig. 21 in the form of C_1, lift coefficient, verse angle of attack, α. Included are Xfoil predictions. For $Re = 75,000$, the three port sets show reasonable accord although the root tappings generally indicate lower loading at higher lift coefficients then port sets A and B. Numerical predictions are somewhat higher than experimental, but the lift curve shape is reasonably consistent. The plots, both numerical and experimental, are seen to exhibit several breaks, not uncommon at low Reynolds numbers. Increasing the Reynolds number to $\geq 100,000$ significantly increases the linearity of the plots and improves agreement between the numerical results and experiment. Concurrence between ports A and B for $Re = 100,000$ and 150,000 is close.

To investigate the junction flow in which tappings C were immersed, the side wall boundary layer was estimated using a boundary layer mouse consisting of 18 miniature total head probes. The survey was performed without the wing in place just upstream of the wing's mounting location. Resulting profiles as well as the estimated displacement thickness (δ^*) are presented in dimensional and nondimensional form (see Fig. 22). Although the survey lacked resolution close to the wall, the profile appears turbulent. Values of δ^*/δ are between the ideal values for laminar and turbulent boundary layers. As may be expected, the wall boundary layer thinned with increasing Reynolds number and reduced from approximately 17 mm to 14 mm. To establish the potential junction flow regime, the Reynolds number based on displacement thickness, Re_{δ^*}, was calculated. Analysis yielded values of $Re_{\delta^*} = 3851$ ($Re = 75,000$), $Re_{\delta^*} = 4569$ ($Re = 100,000$), $Re_{\delta^*} = 5176$ ($Re = 150,000$) and $Re_{\delta^*} = 5258$ ($Re = 200,000$). These values are consistent with a turbulent junction flow [10].

Conclusions

An investigation into the effect of pressure port location and orientation is presented. Data for Reynolds numbers of 75,000, 100,000, 150,000, and 200,000 are presented. A 16%-thick S8036 profile was used in the study. Effects of streamwise, inclined, and root taps were explored. Presented data include pressure plots, lift coefficients, and surface flow visualization. Included for comparison are numerical results generated using Xfoil.

The data show good agreement between experiment and Xfoil for most cases; most disagreement is in the location and extent of the laminar separation bubble. The results show that the streamwise taps may cause premature transition depending on the test Reynolds number and wing incidence. For a given angle of attack, agreement between the streamwise and inclined pressure ports improved with Reynolds number, while for a fixed $Re \leq 100,000$, the accord improved with wing incidence. Tappings at the root generally indicated reduced pressure compared to those along the span, although agreement between all three tap locations was reasonable downstream of the bubble reattachment. As cited in the literature, the effect of increasing Reynolds number was to shorten the laminar bubble, not by altering the location of laminar separation but by earlier transition and reattachment. Incidence was noted to move the bubble toward the leading edge and reduced its length moderately.

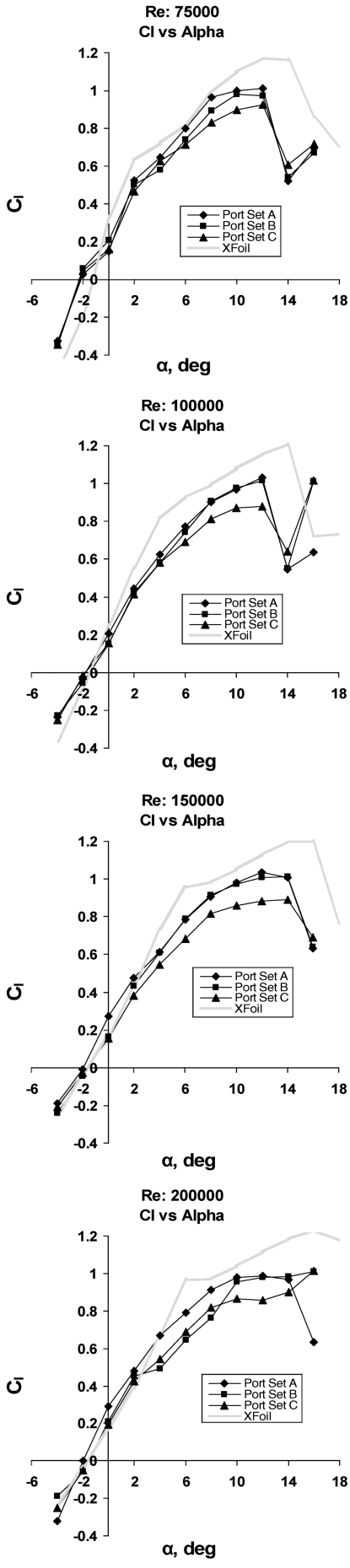

Fig. 21 Effect of Reynolds number and port location on calculated lift coefficients.

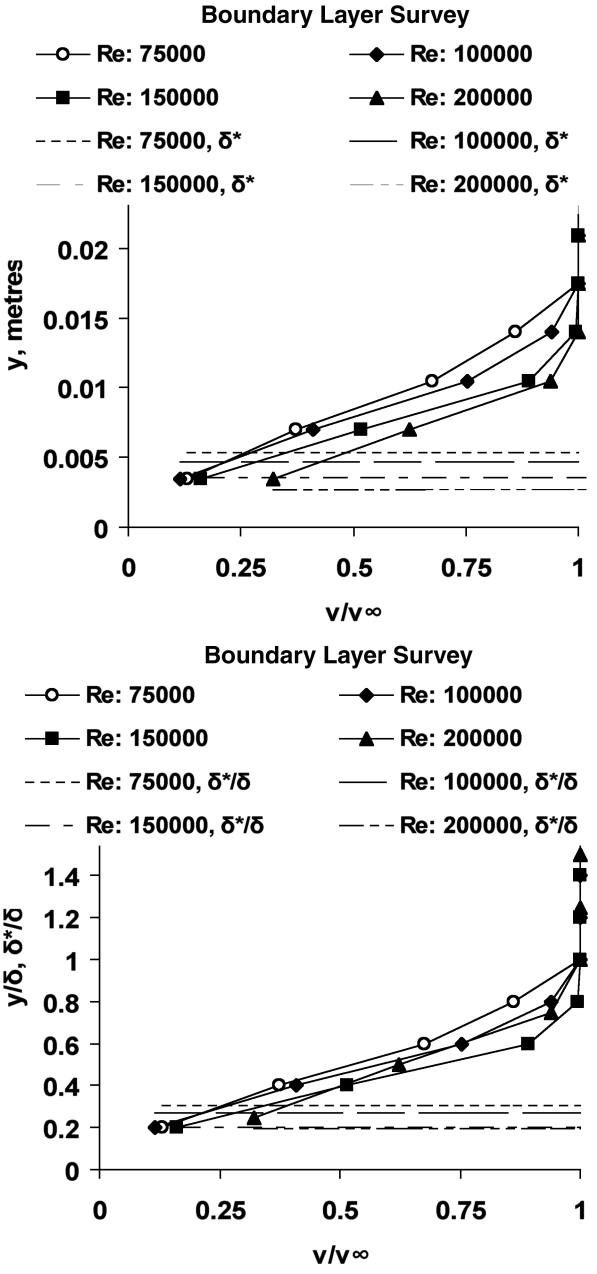

Fig. 22 Wind-tunnel wall boundary layer properties measured upstream of model location. Dimensional (upper figure) and reduced by boundary layer thickness (lower figure).

Acknowledgment

The authors would like to acknowledge support from the Arizona/NASA Space Grant Undergraduate Research Program for Evan Cooper during the conduct of this research. The authors would like to thank Lance Kimbrough for the Fluent™ computations.

References

[1] Lissaman, P. B. S., "Low-Reynolds-Number Airfoils," *Annual Review of Fluid Mechanics*, Vol. 15, 1983, pp. 223–239. doi:10.1146/annurev.fl.15.010183.001255

[2] Weiburst, E., Bertelrud, A., and Ridder, S. O., "Experimental Investigation of Laminar Separation Bubbles and Comparison with Theory," *Journal of Aircraft*, Vol. 24, No. 5, 1987, pp. 291–297.

[3] Hsiao, F. B., and Hsu, C. C., "Numerical Prediction of Aerodynamic Performance for Low Reynolds Number Airfoils," *Journal of Aircraft*, Vol. 26, No. 7, 1989, pp. 689–691.

[4] Roberts, W. B., "Calculation of Laminar Separation Bubbles and Their Effect on Airfoil Performance," *AIAA Journal*, Vol. 18, No. 1, 1980, pp. 25–31.

[5] Schmidt, G. S., and Mueller, T. J., "Analysis of Low Reynolds Number Separation Bubbles Using Semiempirical Methods," *AIAA Journal*, Vol. 27, No. 8, 1989, pp. 993–1001.

[6] Torres, G. E., and Mueller, T. J., "Low-Aspect-Ratio Wing Aerodynamics at Low Reynolds Numbers," *AIAA Journal*, Vol. 42, No. 5, 2004, pp. 865–873.

[7] Pelletier, A., and Mueller, T. J., "Low Reynolds Number Aerodynamics of Low Aspect Ratio Wings," AIAA Paper 99-3182, 1998.

[8] Prazak, M. W., and Mueller, T. J., "Hydrogen Bubble Visualization of the Flow over a Thin Wing at Chord Reynolds Numbers From 12,000 to 21,000," *8th International Symposium on Flow Visualization*, 1998.

[9] Kline, S. J., and McClintock, F. A., "Describing Uncertainties in Single Sample Experiments," *Mechanical Engineering*, Jan. 1953, pp. 3–8.

[10] Simpson, R. L., "Junction Flows," *Annual Review of Fluid Mechanics*, 2001, pp. 415–443. doi:10.1146/annurev.fluid.33.1.415

[11] Squire, L. C., "The Motion of a Thin Oil Sheet Under the Steady Boundary Layer on a Body," *Journal of Fluid Mechanics*," Vol. 11, Sept. 1961, pp. 161–179. doi:10.1017/S0022112061000445

[12] Winkelman, A. E., and Barlow, J. B., "Flowfield Model for Rectangular Planform Wing Beyond Stall," *AIAA Journal*, Vol. 18, No. 8, 1980, pp. 1025–1026.